Polymer Chemistry

PAPER

View Article Online
View Journal | View Issue



Cite this: *Polym. Chem.*, 2019, **10**, 4346

# Hyperbranched phosphorus flame retardants: multifunctional additives for epoxy resins†

Alexander Battig, ‡[a] Jens C. Markwart,‡[b,c] Frederik R. Wurm *[b] and Bernhard Schartel *[a]

Received 21st May 2019,
Accepted 2nd July 2019

DOI: 10.1039/c9py00737g

rsc.li/polymers

We successfully synthesized multifunctional P-based hyperbranched polymeric flame retardants (*hb*-FRs) with varying oxygen-to-nitrogen (O : N) content and characterized them *via* $^{1}$H and $^{31}$P NMR and GPC. Their miscibility in epoxy resins (EP) and impact on glass-transition temperatures ($T_g$) were determined *via* differential scanning calorimetry (DSC). Using thermogravimetric and evolved gas analysis (TGA, TG-FTIR), pyrolysis gas chromatography/mass spectrometry (Py-GC-MS), hot stage FTIR, flammability tests UL-94 and LOI, fire testing *via* cone calorimetry, residue analysis *via* scanning electron microscopy (SEM) and elemental analysis, detailed decomposition mechanisms and modes of action are proposed. *hb*-polymeric FRs have improved miscibility and thermal stability, leading to high FR performance even at low loadings. Polymeric, complex FRs increase flame retardancy, mitigate negative effects of low molecular weight variants, and can compete with commercial aromatic FRs. The results illustrate the role played by the chemical structure in flame retardancy and highlight the potential of *hb*-FRs as multifunctional additives.



## Introduction

Polymeric materials are pervasive throughout almost all aspects of modern life. Their tunable properties promote a wide range of applications, from packaging, transport, and construction to consumer electronics, automotive, and aeronautics. In particular, high-performance polymers are increasingly used to reduce weight and improve fuel efficiency in aviation and automobiles, and their material properties are paramount to their effective use. However, plastics are intrinsically flammable and carry a large fire load, consequently prompting the use and continued research into flame retardants (FRs). Due to environmental and toxicological concerns,[1] efforts into developing halogen-free alternatives to improve safety and reduce risks have led to the formulation of effective phosphorus-based FRs (P-FRs).[2–5]

Moreover, there exists a trend towards polymeric FRs, as the blooming out or leaching of low molar mass FRs is undesirable in consumer products.[6] Low molar mass FRs usually possess low thermal stability, thus limiting their processability. Furthermore, the overlap between the decomposition temperatures of the FR and matrix is crucial to achieving good performance.[7,8] In comparison, oligomeric or polymeric FRs are more effective due to their increased thermal stability which leads to improved chemical interactions during decomposition, yielding higher char yields and better overall flame retardancy.[9,10] In addition, FRs with novel architectures have been investigated, highlighting the impact of the complex chemical structure on the mechanical properties and glass-transition temperature ($T_g$) of the polymer matrix.

One group of polymers which has the potential to merge the approaches of utilizing high molar mass and complex molecular architecture is hyperbranched (*hb*) polymers. *hb* polymers are a group of specialized macromolecules that exhibit a high branching density and are more easily synthesized *via* a one-pot synthesis than other complex polymers.[11,12] A wide array of synthesis routes and applications has been extensively investigated.[13–15]

Due to their unique characteristics, these complex macromolecules have found use in the biomedical field,[16–18] and recently, they have been proposed as FRs for polymers.[19–21] *hb*

[a]*Bundesanstalt für Materialforschung und -prüfung (BAM), Unter den Eichen 87, 12205 Berlin, Germany. E-mail: bernhard.schartel@bam.de*
[b]*Max Planck Institute for Polymer Research, Ackermannweg 10, 55128 Mainz, Germany. E-mail: wurm@mpip-mainz.mpg.de*
[c]*Graduate School Materials Science in Mainz, Staudinger Weg 9, 55128 Mainz, Germany*

†Electronic supplementary information (ESI) available: NMR spectra (Fig. S1–S7); polymerization study (Table S1); DSC results (Table S2); TGA results of *hb*-FRs (Table S3); hydrolysis decomposition (Scheme S1); elimination decomposition (Scheme S2); inter- and intramolecular decomposition (Scheme S3); sulfur decomposition (Scheme S4); mass spectra of Py-GC-MS (Fig. S8–15); surface etching (Fig. S16); DSC (Fig. S17 and 18); TGA results of EP-*hb*-FRs (Table S4); condensed phase FTIR (Fig. S19 and Table S5); LOI & UL-94 measurements (Table S6); MARHE & FIGRA of cone calorimeter (Table S7); CO-yields (Fig. S20 and Table S8); residue analysis (Fig. S21). See DOI: 10.1039/c9py00737g

‡These authors contributed equally.

flame retardants (*hb*-FRs) combine the potential of polymeric FRs with the advantages of complex geometries.[22,23] Their high molar mass and complex architecture lead to high solubility and miscibility with other materials.[24] Chiefly among *hb*-FRs, *hb*-polyphosphoesters have been recently proposed as effective FRs,[25] also in epoxy resins (EP).[26] Additionally, phosphorus (P) and nitrogen (N) containing *hb*-FRs have been investigated,[27,28] as the synergistic qualities of P–N compounds have been widely discussed.[29,30]

In a recent study, we have investigated the flame retardancy effect of P-FRs by systematically varying the structure, namely phosphates, phosphoramidates, phosphorodiamidates, and phosphoramides, and have proven the differences in the decomposition mechanism and mode of action.[31]

In this article, we synthesized *hb*-FRs from the previously investigated corresponding monomeric FRs by a radical $A_2$ + $B_3$ thiol–ene polyaddition (Scheme 1) and investigated their decomposition mechanism. The aim is to compare the FR potential of *hb*-FRs with varying P–O and P–N contents, and the high molar mass variants are compared to their monomers in terms of flame retardancy mechanisms, mode of action, and efficacy in epoxy resins. The $A_2$ + $B_3$ strategy was chosen due to its ease of synthesis and potential for up-scaling.[32,33] As P–O and P–N-bonds possess different stabilities and degradation pathways, an optimized FR performance can be obtained by a precise synthesis of P-FRs.[31]

However, the polymerization process alters the end-group functionality and may affect gas-phase activity. It is unclear which flame-retardant affects the *hb* polymeric variants of previously investigated P-FRs. Moreover, the role of complex molecular architecture in the FR's chemical mechanism remains unclear. With this study, investigating the decomposition pathway of distinctively different *hb*-FRs and their mode of action in EP becomes possible, allowing for a deeper understanding of these multifunctional additives as effective FRs for high-performance polymers. Crucially, the material properties of epoxy resins must be conserved, and by comparing these aliphatic *hb*-FRs to a state-of-the-art, commercially available benchmark FR, their performance can be more accurately estimated. While there have been many reports on P-FR formulations for epoxy resins,[34] of which some studied one type of *hb*-FR,[35,36] this study aims at investigating four high-molar mass *hb* P-FRs with systematically varying P–O and P–N contents which are able to retain the material properties of DGEBA-based EP. The results of material and flame retardancy studies aid in optimizing future design of P-FRs.

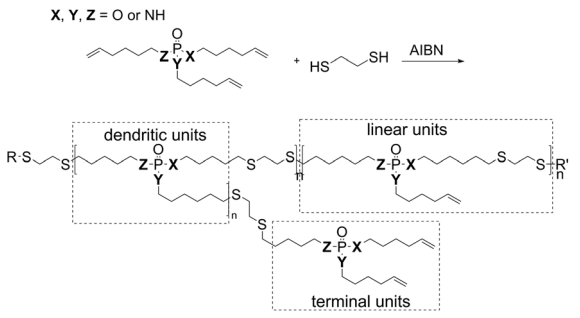


**Scheme 1** Synthesis of *hb*-FRs *via* an $A_2$ + $B_3$ thiol–ene polyaddition, and schematic representation of dendritic, linear, and terminal units of the *hb*-structure.

## Results and discussion

### Hyperbranched flame retardants (*hb*-FRs)

**Chemical synthesis and structure identification.** The influence of the P–O *vs.* P–N ratio on the FR efficiency of low molecular weight P-FRs has been studied recently.[38] To explore the influence of polymeric materials in comparison with monomeric materials, we extended this systematic library with the respective *hb*-polymers. *hb*-Polyphosphoramide (**1**), *hb*-polyphosphorodiamidate (**2**), *hb*-polyphosphoramidate (**3**), and *hb*-polyphosphate (**4**) were synthesized starting from the respective $B_3$-monomers in a radical thiol–ene polyaddition using 1,2-ethanedithiol as an $A_2$-comonomer and AIBN followed by precipitation into *n*-hexane or toluene (Scheme 1). The successful $A_2$ + $B_3$ polymerization was indicated by a reduction in the double-bond resonances in the $^1$H NMR spectra and the detection of a new singlet at 2.71 ppm and a triplet at 2.55 ppm (see the ESI†). By these procedures, all P-FRs were easily available up to at least 80 g with standard university lab equipment. Fig. S1–S3† show the $^1$H NMR spectra of the *hb*-polymers with varying oxygen-to-nitrogen (O : N) ratios. The spectrum of the monomeric phosphate in Fig. 1a highlights the change from the monomeric to polymeric structure. Here, the appearance of a $CH_2$ group (triplet) at 2.55 ppm signified a successful polymerization, as it corresponds to the methylene group adjacent to the thioether. The singlet at 2.71 ppm belongs to the two methylene groups between the two thioether linkages. The signals from 1.70 to 1.38 ppm were attributed to the methylene groups of the alkyl chain. Fig. S4–S7† show the $^{31}$P {H} NMR spectra of the hyperbranched polymers with varying O : N ratios. The resonance of the P-atom shifted depending on its chemical surroundings to lower field with increasing nitrogen content surrounding P (from 17.13 ppm for **1** to −0.66 ppm for **4**).

As an $A_2$ + $B_3$ polymerization can produce both cross-linked and soluble *hb*-polymers,[24] depending on the polymerization conditions and monomer feed ratios, we optimized the polymerization conditions using **4** as an example. Table S1† summarizes the conditions which were varied to produce soluble polymers compared to cross-linking, yield and molecular weights for different monomer feed ratios. For all molar feed ratios up to 8 : 5 (thiols of the $A_2$ *vs.* double bonds of the $B_3$), cross-linking was observed. For molar ratios 5 : 9, 5 : 10 and 5 : 11, no gelation occurred, and soluble polymers were obtained. The molecular weights decreased with increasing excess of the $B_3$-monomer. Also, the 5 : 9 ratio did not always prevent cross-linking, most probably due to variations in the mixing process by the mechanical stirrer. GPC elugrams also sometimes exhibited shoulders to lower elution volumes, indi-

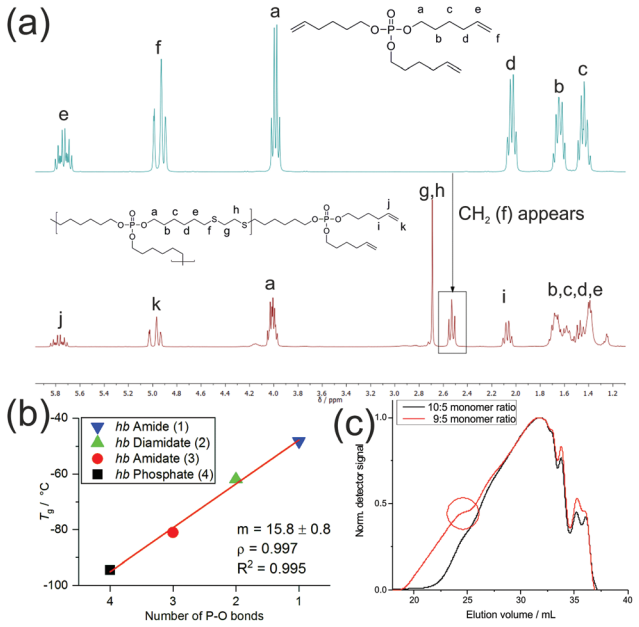


**Fig. 1** (a) $^1$H NMR (300 MHz in $CDCl_3$ at 298 K) of tri(hex-5-en-1-yl) phosphate (top) and *hb*-polyphosphate (**4**) (bottom). The appearance of the singlet (g and h) and the triplet (f) signifies successful thiol–ene reactions. (b) Relationship between the number of P–O bonds in *hb*-FRs and their glass transition temperature ($T_g$) *via* differential scanning calorimetry (DSC). Linear fit (red line) with a slope (*m*), Pearson's correlation coefficient ($\rho$) and its square ($R^2$). (c) GPC-elugrams (RI detection) of $A_2 + B_3$ polymerization to **4** at different monomer feed ratios. The red circle indicates the beginning of gelation.

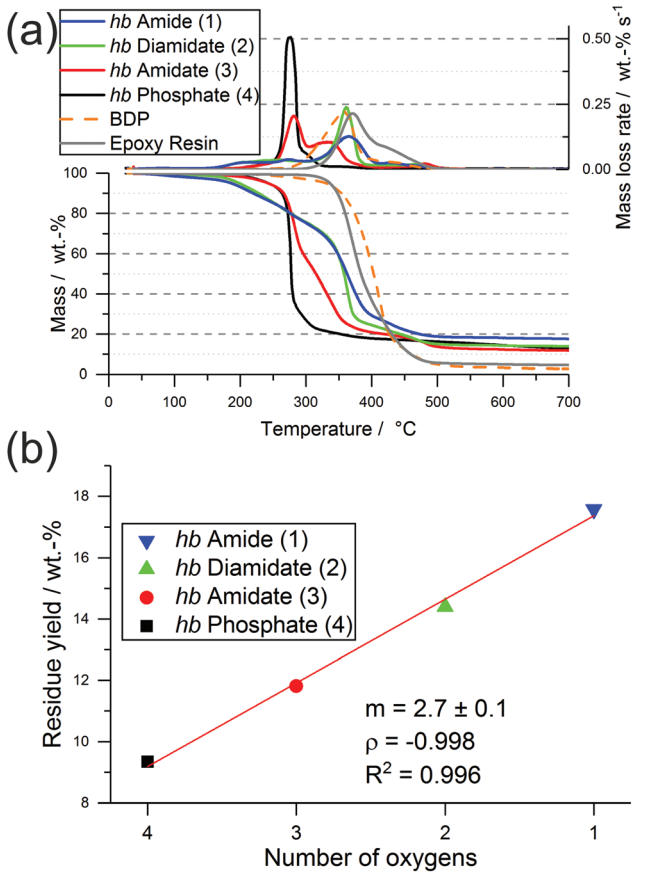


**Fig. 2** Pyrolysis investigations *via* thermogravimetric analysis (TGA) of hb-FRs: (a) mass loss (bottom) and mass loss rate (top) over *T* of *hb*-FRs; (b) linear relationship between the number of oxygen atoms in the P-binding sphere of *hb*-FRs and their residue yield at 700 °C (red line: linear fit; *m*: slope; $\rho$: Pearson's correlation coefficient or PCC; $R^2$: PCC squared).

cating an onset of gelation under these conditions (Fig. 1c). Although the 5 : 9 ratio provided the highest molecular weights after 24 h of polymerization, the broadest molar mass dispersity with *ca.* $M_w/M_n$ = 12 was obtained. The 5 : 11 and 5 : 10 ratios both prevented gelation and resulted in lower molar masses. We chose the 5 : 10 ratio for the following studies as it prevented gelation effectively and resulted in higher molar masses than the 5 : 11 ratio. All polymers were obtained in yields of 76–89% as off-white and viscous oils.

**Material properties.** The glass-transition temperatures ($T_g$) of the *hb*-polymers were investigated *via* differential scanning calorimetry (DSC), indicating the fully amorphous behavior of all synthesized polymers (Fig. S17 and Table S2†). The glass-transition temperature increased linearly with the reduction of P–O bonds, *i.e.* an increase of P–N bonds, in the *hb*-polymer structure (Fig. 1b). The $T_g$ of the *hb*-polyphosphate was detected at −94 °C and increased by approx. 16 °C for each subsequent N bound to P to *ca.* −48 °C for **1**.

**Pyrolysis.** The decomposition behaviors of the *hb*-FRs under pyrolytic conditions were investigated using TGA (Fig. 2a and Table S3†). The mass loss curve of the *hb*-phosphate (**4**) exhibited a main single decomposition step at 274 °C (81 wt% mass loss) with a gradual decomposition thereafter. The *hb*-amidate (**3**) displayed a mass loss curve similar to **4**: its onset temperature ($T_{5\%}$) and temperature of maximum mass loss rate ($T_{max}$) were in a similar range (242 °C and 281 °C, respectively); however, the main decomposition step presented an additional shoulder that extended over a range of approx. 40 °C and peaked at 335 °C. Additionally, a small decomposition step (approx. 8 wt%) appeared at 481 °C. The *hb*-diamidate (**2**) exhibited a decomposition step which extended over a large temperature range from $T_{5\%}$ at 194 °C to just before $T_{max}$ at 359 °C. Similarly, the *hb*-amide (**1**) also showed a steady decomposition between $T_{5\%}$ at 190 °C until shortly before $T_{max}$ at 361 °C. For both **1** and **2**, a small decomposition step (approx. 10 wt%) occurred at 463 °C and 428 °C, respectively. The amount of residue increased from 11.2 wt% for **4** to 17.6 wt% for **1**.

Interestingly, the residue amount after pyrolytic decomposition increased with increasing N content by approx. 2.7 wt%, and Fig. 2b illustrates the linear increase between the number of O in the P-binding sphere and the residue yield. The increase in residue yield with increasing P–N bonds in the *hb*-FRs results from the formation of thermally stable intermediates that decompose over a broad temperature range. When comparing **3** and **4**, the replacement of a P–O bond with a P–N bond increased residue yield and introduced an additional

 

decomposition step at elevated temperatures. When comparing **1** and **2** to **3** and **4**, the mass loss behavior changed drastically from a single-step decomposition with a shoulder to a multi-step decomposition over a large temperature range, pointing to a crucial influence of the number of P–N bonds in the polymer on its decomposition pathway.

To better understand the decomposition mechanisms of the FRs under pyrolytic conditions, the materials were investigated *via* evolved gas analysis using TGA-FTIR (Fig. 3a–d) and pyrolysis gas chromatography/mass spectrometry (Py-GC/MS) (Fig. 4). The evolved gas FTIR spectra of decomposition products correspond to specific decomposition steps during pyrolysis of *hb*-FRs. For *hb*-FRs, either 5-hexene-1-ol and/or 5-hexene-1-amine was detected during the decomposition, depending on the O : N ratio, which correlates well with previous investigations for low molar mass P-FRs.[31] 5-Hexene-1-ol was identified *via* the vibration band at 1054 $cm^{-1}$ from the stretching vibration of (C–O). 5-Hexene-1-amine was identified *via* the stretching vibration band at 1068 $cm^{-1}$ from (C–N) and the wagging deformation band at 769 $cm^{-1}$ from (N–H). Additionally, 1,5-hexadiene was identified as a decomposition product (*via* a β-elimination) for all *hb*-FRs *via* the bands at 3082 $cm^{-1}$ from unsaturated hydrocarbons and those at 1642 $cm^{-1}$, 1452 $cm^{-1}$, 998 $cm^{-1}$ and 917 $cm^{-1}$ belonging to various C–H vibrations of the hexene moiety, which were also observed in 5-hexene-1-amine and 5-hexene-1-ol. Interestingly, at $T > 330$ °C, all spectra showed few if any bands for unsaturated hydrocarbons (bands > 3000 $cm^{-1}$). Furthermore, **2**, **3**,

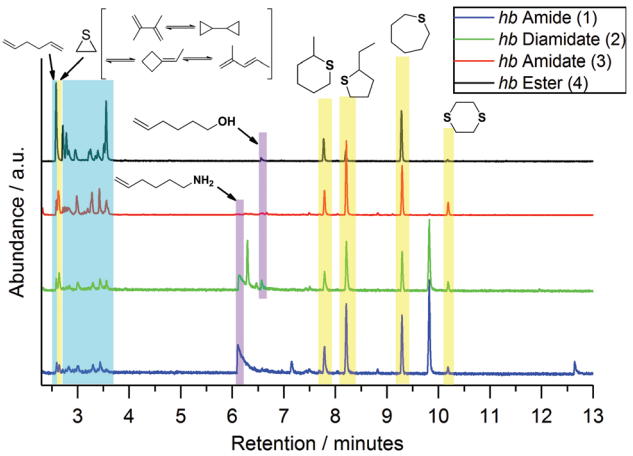


**Fig. 4** Ion chromatograms of *hb*-FRs from pyrolysis gas chromatography/mass spectrometry (Py-GC-MS) measurements. Highlighted areas correspond to relevant compounds identified *via* the NIST14 MS library.

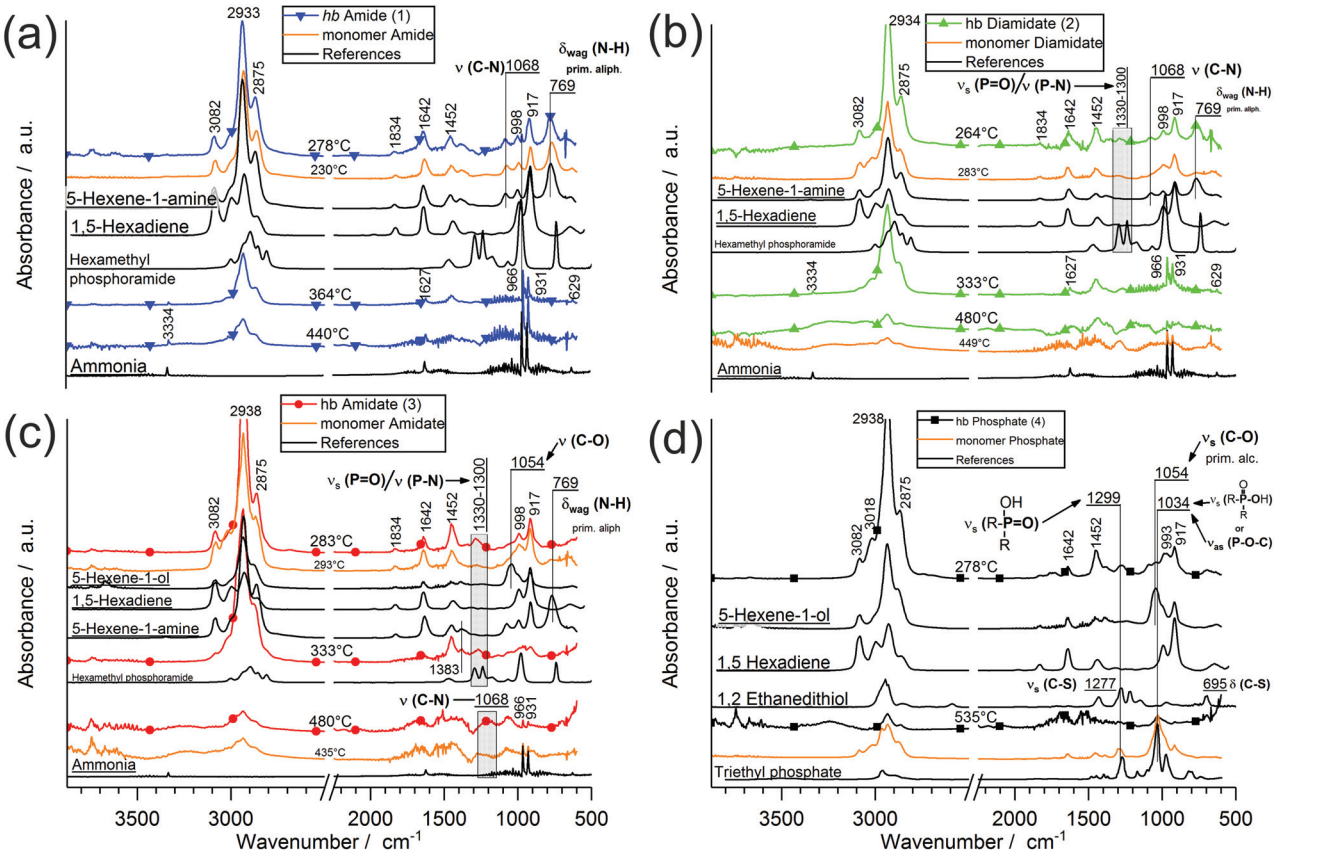


**Fig. 3** Evolved gas analysis *via* FTIR (TG-FTIR) of *hb*-FRs: (a–d) FTIR spectra of *hb*-FRs at specific decomposition steps, their monomeric variants (orange) and comparative spectra.

and **4** exhibited the production of a P-species at $T$ = 260–280 °C: for **2** and **3**, the bands at 1330–1300 $cm^{-1}$ from the overlapping stretching vibrations of P═O or P–N, and for **4**, the bands at 1299 $cm^{-1}$ from the stretching vibration $R_2$–(P═O)–OH, and 1034 $cm^{-1}$ from $R_2$–(P–OH)═O or the stretching vibration of (P–O–C). During the decomposition of the *hb*-FRs with P–N bonds, the evolution of ammonia at $T$ = 330–360 °C and temperatures above 440 °C was identified by the bands at 3334 $cm^{-1}$, 1642 $cm^{-1}$, 966 $cm^{-1}$, 931 $cm^{-1}$, and 629 $cm^{-1}$.

The FTIR spectra, TGA mass loss curves, and residue amounts after pyrolysis point toward a certain behavior during pyrolysis: all units of the *hb*-FR undergo several types of decomposition reactions, and several mechanisms occur simultaneously or in tandem with one another. A general decomposition pathway is described in Scheme 2, and hydrolysis (Scheme S1†), elimination (Scheme S2†), and intra- or intermolecular reactions (Scheme S3†) are described more in depth in the ESI.†

For Py-GC/MS, μg samples were pyrolyzed at a specific temperature and the evolved gases passed through a GC separation column and an MS detector. Measurements at 500 °C (Fig. 4) revealed additional information on the decomposition mechanism of *hb*-FRs: the production of 1,5-hexadiene was identified by the mass spectrum at 2.6 min (Fig. S8†) and the signals at retention times of 2.7–3.7 min (areas highlighted in blue) were assigned to various $C_6H_{10}$-species formed by the high-temperature rearrangement of 1,5-hexadiene. Moreover, 5-hexene-1-amine and 5-hexene-1-ol (areas highlighted in purple) were observed at retention times of 6.1 min (Fig. S10†) and 6.6 min (Fig. S11†), respectively. Additionally, all *hb*-FRs formed cyclic sulfur-containing compounds (areas highlighted in yellow). The mass spectra of all *hb*-FRs at retention times of 2.63 min (corresponding to thiirane), 7.8 min (corresponding to 4-methylthiane), 8.2 min (corresponding to 2-ethylthiophane), 9.3 min (corresponding to thiepane), and 10.2 min (corresponding to 1,4-dithiane) are summarized in Fig. S9, S12, S13, S14 and S15,† respectively. A mechanism leading to the production of these products is proposed in Scheme S4.†

## Flame retardant epoxy resins (EP-FRs)

**Material properties.** The miscibility of **1** and **4** with EP was studied from 0 up to 40 wt%: all samples were translucent and showed no sign of macro-phase separation (Fig. 5a). The miscibility of **4** with EP is further supported by SEM and TEM images (Fig. S21†). A homogeneous surface of a section of EP with 10 wt% of **1** is shown in Fig. S16a.† There is no obvious indication of phase separation. Fig. S16b† displays the surface of EP fractured under cryogenic conditions and etched in dichloromethane according to the method of Meng *et al.*,[37] who studied the phase separation within EP by fracturing the sample under cryogenic conditions and etching it in dichloromethane for thirty minutes. The filler used by Meng *et al.* was soluble in dichloromethane like **4** used in this experiment. The cut block surface which was etched in dichloromethane is illustrated in Fig. S16c† and showed no signs of phase separation as indicated by the absence of grooves on the surface. These results are supported by a sample stained with ruthenium tetroxide and analyzed by TEM (Fig. S16d†), in which a homogeneous surface is visible, indicating no sign of phase separation. Differential scanning calorimetry (DSC) measurements (Fig. S17†) presented only one glass-transition temperature ($T_g$), further supporting the absence of macro phase separation.

All *hb*-FRs were used as additive flame retardants and under the curing conditions no side-reactions of the phosphoramide-bond with the epoxy were reported.[31] The impact of *hb*-FRs on the $T_g$ of EP (Fig. S18†) is presented in Fig. 5b, and the change of $T_g$ relative to EP is noted. When comparing the $T_g$ of EP with the monomer of **4** with the $T_g$ of EP-**4**, the *hb*-FR exhibited a relative increase of 17%, which showcases the decreased effect of *hb*-FRs over their low molecular weight P-FR counterparts. All *hb*-FRs except **1** lowered $T_g$ of EP at a similar level to the benchmark material BDP, *i.e.* by 14%. **1** had the lowest impact on $T_g$ compared to the other FRs, lowering $T_g$ by only 8% to 142.5 °C. The $T_g$ values are ordered **4** < **3** < **2** < **1**, following the trend visible in the $T_g$ of pure *hb*-FRs. It should be noted that *hb*-FRs are composed of aliphatic hydrocarbons as opposed to BDP, which contains aromatic rings. The reduced effect on $T_g$ that these aliphatic FRs exhibit is comparable to that by aromatic compounds, which speaks for the ability of *hb*-FRs to mitigate the plasticizing effect of conventional aliphatic FRs. The *hb*-polymers present significantly higher $T_g$ values in EP than their monomeric analogues (16–21% increase),[31] highlighting their character as multifunctional FRs.

**Pyrolysis – mass loss and evolved gas analysis.** To understand the decomposition behavior of EP-*hb*-FRs, the mass loss and evolved gas analysis of the pyrolytic decomposition was investigated *via* TGA coupled with gas FTIR. The results are summarized in Table S4.† The mass loss and mass loss rate curves of EP and EP-FRs (Fig. 6a) and the change in residue yields at 700 °C (Fig. 6b) signify a significant change in the decomposition of EP when *hb*-FRs are added, providing evidence for their interaction during pyrolysis. EP began to decompose at $T_{5\%}$ = 338 °C and reached $T_{max}$ at 372 °C. The material decomposed in a single main step equal to a mass loss of 62 wt%, with a shoulder beginning at 424 °C equal to a mass loss of 33 wt%. The residue at 700 °C was 4.5 wt%. The mass loss and evolved gas analysis of the resin DGEBA-DMC has been previously reported and will not be discussed in further detail here.[38,39] The resin with the benchmark material BDP (EP-BDP) decomposed in a single step with a shoulder, analogously to EP. However, $T_{5\%}$ was 33 °C and $T_{max}$ was 15 °C lower than that of EP, which is attributed to a reduction in cross-linking density of the flame retardant EP system. The shoulder starting at 423 °C showed a lower decomposition rate compared to EP. The mass loss at $T_{max}$ increased to 75 wt% and decreased to 16 wt% at the shoulder. This results from the interaction of BDP with the decomposing matrix, more closely the binding of phenol-derivatives and cycloalkanes which exhibit a maximum in the production rate in this temperature

 

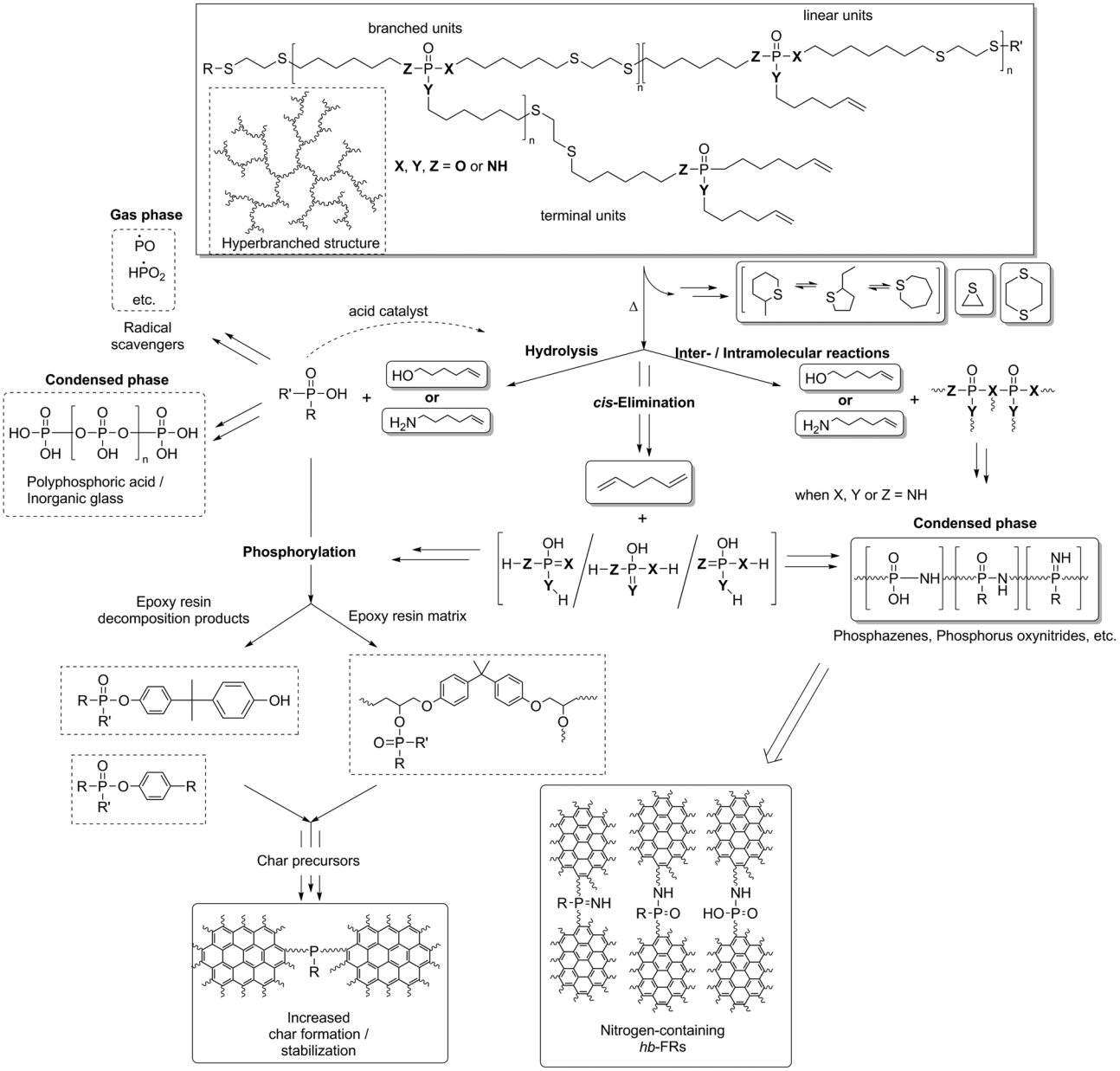


**Scheme 2** Proposed decomposition mechanism of *hb*-FRs and FR interaction with EP during thermal decomposition of EP-*hb*-FRs. Solid squares: identified products (TG-FTIR, hot stage FTIR, *etc.*).

range.[9] This interaction also explains the increased residue yield of EP-BDP, which nearly doubled to 8.2 wt%.

All EP-*hb*-FRs exhibited a similar decomposition behavior to EP-BDP: $T_{5\%}$ was lower than EP by an average of approx. 47 °C, while $T_{max}$ was lowered by an average of approx. 21 °C. The residue yields of the EP-*hb*-FRs varied depending on the O : N ratio of the *hb*-FRs (Fig. 6b): EP with *hb*-phosphate (EP-**4**) and EP with *hb*-amidate (EP-**3**) showed a similar residue yield (7.7 and 6.8 wt%, respectively), while EP with *hb*-diamidate (EP-**2**) and *hb*-amide (EP-**1**) exhibited residue yields similar to EP-BDP (8.1 wt% and 8.0 wt%, respectively). Although EP-**3** exhibited a lower residue yield, all *hb*-FRs increased residue yields by the same margin as the benchmark FR, signifying their ability to interact with the decomposing matrix, forming thermally stable residues. The mass loss of *hb*-FRs in EP was strikingly different from their monomeric FR variants: whereas the latter exhibited a mass loss equal to approx. 10 wt% near 220 °C (Fig. 3b, dotted line), all *hb*-FRs are significantly more thermally stable than their low molar mass counterparts in this temperature range and exhibited only minor decomposition.[31] This higher decomposition temperature increased the overlap of FRs and matrix decomposition, leading to higher reactivity and interaction during pyrolysis,[9,40] further illustrating the multifunctional capabilities of *hb*-FRs and the ability

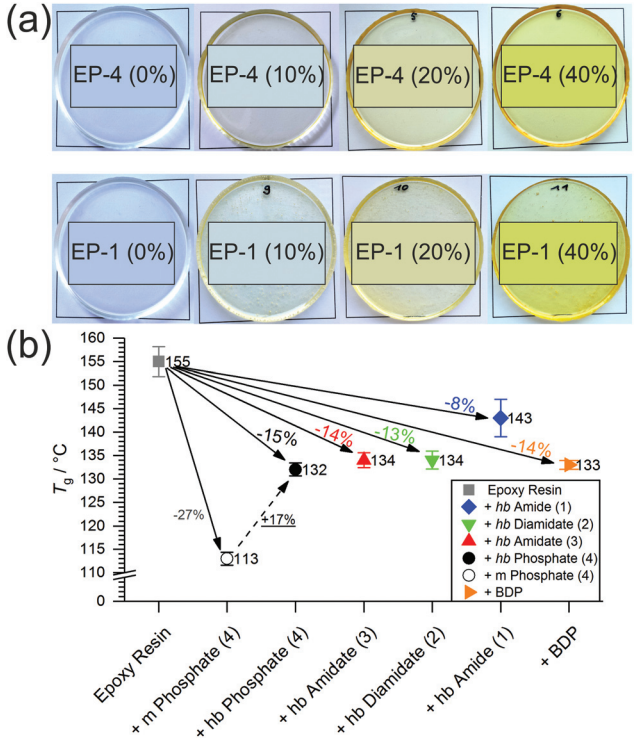


**Fig. 5** (a) EPs with increasing FR loadings (top row: EP-**4**; bottom row: EP-**1**; left to right: 0, 10, 20, 40 wt%), phase separation not visible regardless of loading; (b) $T_g$ values of EP and EP-FRs and change in $T_g$ relative to EP (in %), (dotted line: relative change in $T_g$ from EP with the monomer of **4** to EP-**4**).

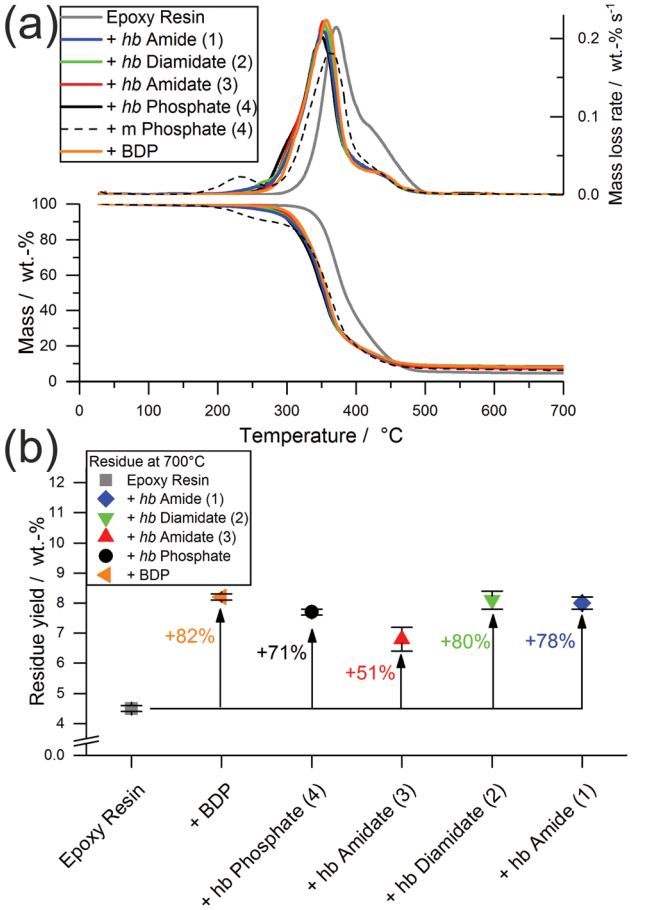


**Fig. 6** (a) Mass loss (bottom) and mass loss rate (top) over $T$ of EP-FRs from TGA measurements (dotted line: EP with the monomer of **4**); (b) residue yields at 700 °C from TGA measurements of EP and EP-FRs and change relative to EP (in %).

of polymeric FRs to overcome the impediments of their monomeric FR variants as well as perform equally to aromatic compounds.

When comparing the FTIR spectra of evolved gases near $T_{5\%}$ for EP-*hb*-FRs with monomeric FR variants in EP (Fig. 7a), the distinct similarities in the spectra indicate analogous decomposition products, namely 5-hexene-1-ol, 5-hexene-1-amine, cyclohexene, 1,5-hexadiene, and acetaldehyde. The spectra of EP-**2**, EP-**3**, and EP-**4** exhibited the (C–O) stretching vibration band at 1054 cm$^{-1}$ assigned to 5-hexene-1-ol. EP-**2** and EP-**3** produced cyclohexene as identified *via* the C–H bending vibration at 1140 cm$^{-1}$. The spectra of EP-**1** showed the (C–N) vibration band of aliphatic hydrocarbons at 1068 cm$^{-1}$ and the (N–H) wagging deformation of primary amines of aliphatic molecules at 769 cm$^{-1}$, pointing to the production of 5-hexene-1-amine. Moreover, the (C=O) stretching vibration at 1730 cm$^{-1}$, corresponding to acetaldehyde, was visible for EP-**1**, EP-**3**, and EP-**4**, while it was concealed under noise for EP-**2**. Acetaldehyde is a product of the decomposition of unreacted epoxide groups from EP.[39] The band at 3082 cm$^{-1}$ belonging to the (C=C) stretching vibration was visible in all EP-*hb*-FR spectra at $T_{5\%}$ and indicated that the decomposition products are unsaturated. When investigating the evolved gas spectra of EP, EP-*hb*-FRs, and EP-BDP at $T_{max}$ (Fig. 7b), all spectra were identical to the spectrum of EP, signifying that EP-*hb*-FRs did not exhibit gas evolvement at this point. This correlates well with the mass loss curves of the *hb*-FRs under pyrolytic conditions (Fig. 2a), as the *hb*-FRs have nearly completely decomposed at the $T_{max}$ of EP. These FTIR spectra provide further evidence that terminal and linear units of the *hb* structure decomposed near $T_{5\%}$ as evidenced by the presence of unsaturated hydrocarbons present solely on these units and 5-hexene-1-ol and/or 5-hexene-1-amine, respectively. As previously mentioned, this can be rationalized by the lower thermal stability of the ω-hexenyl side chains compared to the thiol-linked main chain.

The decomposition pathway is a complex interaction of the FR, the matrix and the decomposition species thereof.[40] The detection of various P-species in the condensed phase (Fig. S19†) confirms that *hb*-FRs interact with the decomposing matrix. The incorporation of P into the residue increases charring *via* enhanced cyclization of the hydrocarbon chains and stabilizes the carbonaceous char by acting as cross-linking points between the polyaromatic hydrocarbons.[41] The proposed mechanism is presented in Scheme 2: the decomposition of *hb*-FRs leads to the formation of O=(P–OH) groups

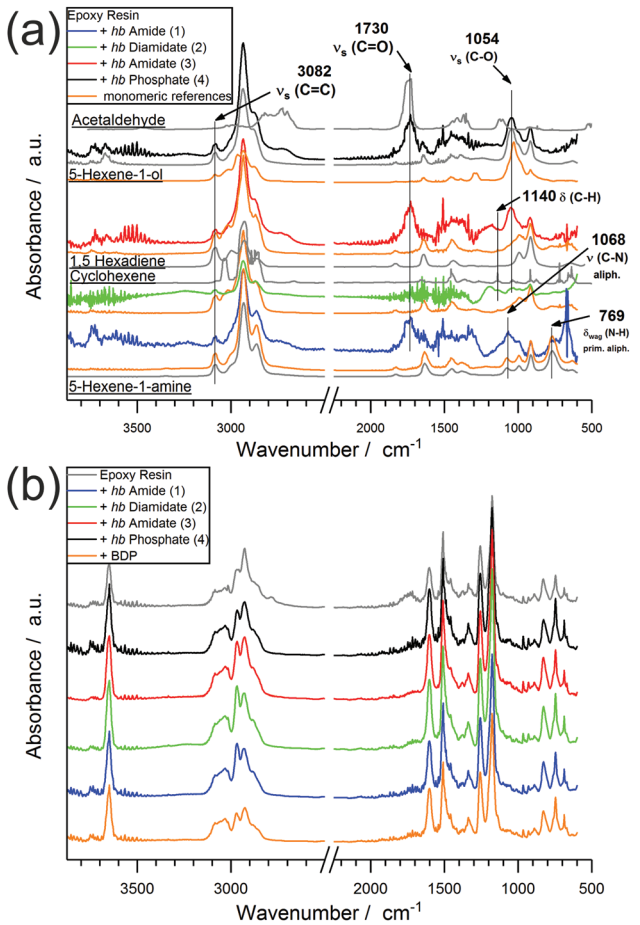


Fig. 7 Evolved gas spectra of EP-*hb*-FRs *via* TG-FTIR at $T_{5\%}$; (orange: monomeric FR spectra at $T_{max}$; gray: comparative spectra) (b) evolved gas spectra of EP and EP-*hb*-FRs *via* TG-FTIR at $T_{max}$.

*via* hydrolysis of the (P–N) or (P–O) bond, respectively, resulting in the production of phosphoric acid and acid derivatives. These P-based acids interact with EP in three ways: acting as acid catalysts for further hydrolysis,[42] aiding in the phosphorylation process of the EP matrix *via* esterification and dehydration,[43] and forming an inorganic glass *via* polyphosphoric acid, thus affording thermal stability to the residue.[7,44] For N-containing *hb*-FRs, the formation of phosphazenes, phosphorus oxynitrides, and other $P_xN_yO_z$ species further increased cross-linking of the aromatic char, and the presence of N can accelerate phosphorylation through synergy.[45–47]

**Fire behavior.** EP and all EP-FRs were investigated for their reaction-to-small-flame behavior *via* UL-94 and LOI (Table S6†) and under forced-flaming conditions in a cone calorimeter to determine their fire load, residue yields, smoke and gas production, and heat release rate (HRR). The HRR of a "steady state" burning polymer is described by the following equations:[48]

$$\mathrm{HRR} = \chi \cdot \theta(t) \cdot (1-\mu) \cdot (h_c^0/h_g) \cdot \dot{q}''_{\mathrm{eff}} \quad (1)$$

$$\dot{q}''_{\mathrm{eff}} = (\dot{q}''_{\mathrm{ex}} + \dot{q}''_{\mathrm{flame}} - \dot{q}''_{\mathrm{rerad}} - \dot{q}''_{\mathrm{loss}}) \quad (2)$$

where $\chi$ is the combustion efficiency, $\theta(t)$ is the time-dependent protective layer effect, $\mu$ is the residue yield, $h_c^0$ is the heat of complete combustion, $h_g$ is the heat of gasification, $\dot{q}''_{\mathrm{eff}}$ is the effective heat flux, $\dot{q}''_{\mathrm{ex}}$ is the external heat flux, $\dot{q}''_{\mathrm{flame}}$ is the heat flux due to thermal feedback, $\dot{q}''_{\mathrm{rerad}}$ is the heat flux from reradiation, and $\dot{q}''_{\mathrm{loss}}$ is the loss of heat flux out of the flame.

The results of the cone calorimeter experiments are summarized in Table 1 and Fig. 8 plots the HRR and total heat released (THR) as functions of time. The shape of the HRR-curves gives insight into the behavior of the material during flaming combustion and highlights the modes of action of the FRs.[49] For EP, the shape was typical of non-charring, thermally intermediately thick samples: after ignition, the material began to decompose with a strong initial increase in the HRR.

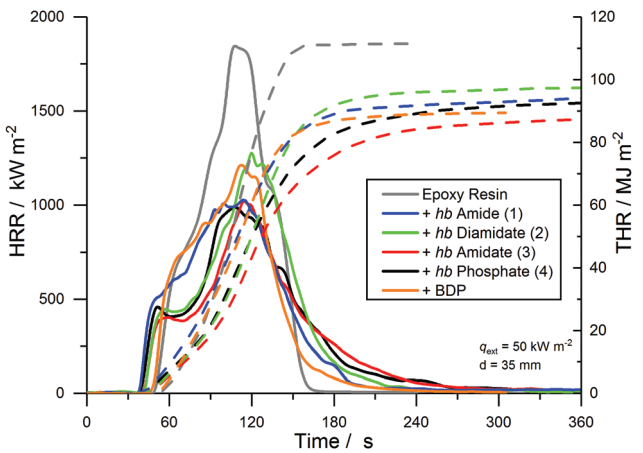


Fig. 8 Heat release rate (HRR, full line) and total heat released (THR, dotted line) over *t* of EP and EP-FRs.

Table 1 Results from cone calorimeter experiments of EP and EP-FRs

| | EP | EP-1 | EP-2 | EP-3 | EP-4 | EP-BDP |
|---|---|---|---|---|---|---|
| THE [MJ m$^{-2}$] | 108.4 ± 2.6 | 95.5 ± 2.3 | 99.1 ± 2.7 | 86.6 ± 0.1 | 89.8 ± 3.0 | 87.5 ± 1.2 |
| PHRR [kW m$^{-2}$] | 1696 ± 180 | 1189 ± 155 | 1325 ± 10 | 1019 ± 17 | 953 ± 41 | 1180 ± 41 |
| Residue [wt%] | 0.7 ± 0.1 | 12.1 ± 2.7 | 7.0 ± 0.1 | 13.6 ± 0.5 | 7.5 ± 0.6 | 3.1 ± 0.2 |
| EHC [MJ kg$^{-1}$] | 26.9 ± 1.0 | 25.5 ± 0.5 | 26.8 ± 0.8 | 25.1 ± 0.1 | 24.3 ± 0.6 | 22.7 ± 0.2 |

THE = total heat evolved (=THR at flame-out).

The quasi-static HRR corresponding to the steady state HRR is marked only by a shoulder and disappears near the peak of heat release rate (PHRR). The peak results from a reduction of $\dot{q}''_{loss}$ caused by the glass wool under the sample preventing heat transfer to the sample holder as the pyrolysis zone approaches. EP had a PHRR of 1696 kW $m^{-2}$ and a total heat evolved (THE = THR at flame-out) of 108.4 MJ $m^{-2}$. It exhibited an effective heat of combustion (EHC = total heat evolved/total mass loss) of 26.9 MJ $kg^{-1}$ and a residue yield of 0.7 wt%. For EP-BDP, the HRR-curve resembled a mixture of thermally thick charring materials and thermally intermediately thick non-charring materials: while it retained the characteristic shape of EP, the addition of a charring mode of action was visible, resulting in a 30% reduction of the PHRR (1180 kW $m^{-2}$). THE and EHC were also 19% and 16% lower than EP (THE = 87.5 MJ $m^{-2}$; EHC = 22.7 MJ $kg^{-1}$), respectively. The residue yield was 3.1 wt%.

All EP-*hb*-FRs reduced the fire load of EP by 9–20% and the PHRR by 22–44% and increased residue yields in the order EP-**2** < EP-**4** < EP-**1** < EP-**3**. EP-**2** showed the lowest residue amount (7.0 wt%) and EP-**3** exhibited the highest amount (13.6 wt%). EP-**3** and EP-**4** displayed the greatest reduction in PHRR and THE, while EP-**1** and EP-**2** did not achieve the same reduction in these indices. Nearly all *hb*-FRs exhibited a plateau-like shape approx. 20–30 s after ignition, which was caused by the formation of a protective char layer on the sample surface, shielding the underlying material from irradiation and reducing the PHRR. Additionally, the release of P-containing volatiles, observed in pyrolysis investigations (Fig. 2), acted in the gas phase as radical scavengers or fuel diluters, thus reducing THE. As combustion continued, the protective layer effect rescinded, and the decomposition of the underlying material increased towards the PHRR. After flame-out, the char layer underwent thermo-oxidation as evidenced by the slow increase of THR over time in the plateau-state at $t > 240$ s.

Petrella-plots are a way to assess fire behavior and flame retardancy:[50] the fire load (THE) is plotted over the fire growth index (PHRR/$t_{ig}$), as THE quantitatively describes heat released but lacks a description of release rate, while PHRR/$t_{ig}$ describes the flashover potential (severity of a fire, or peak heat release potential) but is not quantitative. The Petrella-plot of EP and EP-FRs (Fig. 9) displays that, while the PHRR/$t_{ig}$ of EP was 36 kW $m^{-2}$ $s^{-1}$ and the THE was 109.6 MJ $m^{-2}$, all EP-FRs exhibited a lower PHRR/$t_{ig}$ and THE, as indicated by the shift to the lower left corner of the coordinate system. **2** displayed the lowest flame retardancy, lowering THE by only 10% to 99.1 kW $m^{-2}$ $s^{-1}$ and PHRR/$t_{ig}$ by only 7% to 33.6 MJ $m^{-2}$, while **3** showed the greatest reduction in both THE (21% reduction to 86.6 MJ $m^{-2}$) and PHRR/$t_{ig}$ (31% reduction to 24.9 kW $m^{-2}$ $s^{-1}$). The plot visualizes the ability of **3** and **4** to act more effectively in forced-flaming conditions than **1** and **2**, providing further evidence that a critical O : N ratio determines decomposition behavior due to changes in the flame-retardancy mechanism and mode of action. Moreover, **3** and **4** outperform BDP, providing further evidence that *hb*-FRs can compete with aromatic compounds.

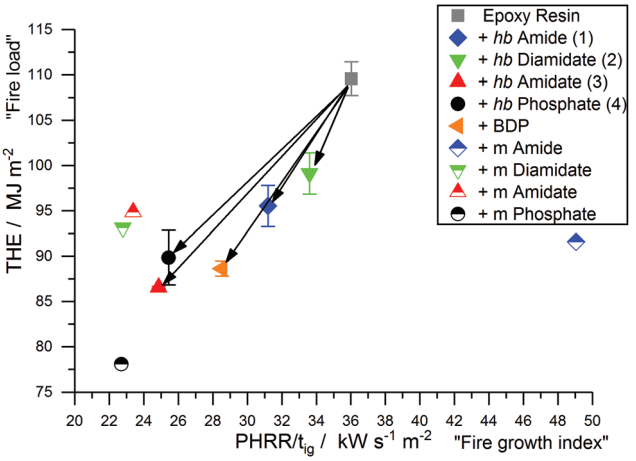


**Fig. 9** Petrella-plot of EP and EP-FRs, assessing fire load (THE) *versus* fire growth (PHRR/$t_{ig}$).

Furthermore, Fig. 9 also visualizes the change in fire behavior from the monomer to polymer: the low molar mass variants exhibited very scattered results, where the monomer of **4** had a very different impact compared to the monomer of **1** in terms of lowering the fire load and fire growth index of EP. Although the *hb*-FRs presented varied results based on their O : N ratio, in general they displayed significantly less disperse values for fire growth and fire load, the result of a more pronounced chemical interaction between the FR and matrix during decomposition.

# Experimental

## Materials

**Chemicals.** All chemicals were purchased from commercial suppliers as reagent grade and used without further purification. The monomers were prepared according to the literature.[31]

## Methods

**NMR.** Nuclear magnetic resonance measurements ($^1$H, $^{31}$P-{H} and $^{13}$C-{H} NMR) were performed on a Bruker Avance (Bruker, Ettlingen, Germany) spectrometer at 250, 300, 500, and 700 MHz on samples solved in deuterated chloroform, deuterated dimethyl sulfoxide or deuterated *N*,*N*-dimethylformamide. Calibration spectra were measured against the solvent signal. All spectra were analyzed using MestReNova 9 (Mestrelab Research S.L., Santiago de Compostela, Spain).

**GPC-MALS.** For gel permeation chromatography with multi-angle laser light scattering online detection (GPC-MALS), a light scattering detector combined with a suitable concentration detector was connected to the output of the GPC columns for the direct determination of the molecular weight. The refractive index increment (d*n*/d*c*) was determined online under the assumption that 100% of the sample mass is injected and elutes from the column. For the P–N containing polymers, DMAc as the mobile phase with 2 g $L^{-1}$ LiBr and

 

2 g $L^{-1}$ TRIS was used. As the stationary phase, a GRAM linear M column with a particle size of 10 μm from PSS Polymer Standards Service GmbH was used. The operation temperature was 60 °C. For the phosphate, the mobile phase was THF. As the stationary phase, three SDV columns with a porosity of $10^6$, $10^4$ and 500 Å and a particle size of 10 μm from PSS Polymer Standards Service GmbH were used. The operation temperature was 30 °C.

**DSC.** For *hb*-FRs, a Mettler Toledo DSC 823e (Mettler Toledo, Columbus OH, USA) was used at a heating and cooling rate of 10 K $min^{-1}$ under a nitrogen atmosphere with a flow rate of 30 ml $min^{-1}$. Three measurements of a heating–cooling–heating cycle were performed. Measurements of the flame retardant epoxy resins were performed on a Netzsch 204 F1 "Phoenix" (Netzsch Instruments, Selb, Germany) using a 5 mg solid sample. Three heating and two cooling runs were performed at a rate of 10 K $min^{-1}$ in the temperature range from −80 to 180 °C for epoxy resins. The $T_g$ of a material was taken as an average of the 2nd and 3rd heating run.

**TGA/TG-FTIR.** Thermogravimetric analysis and evolved gas analysis *via* FTIR measurements were performed on a TG 209 F1 Iris (Netzsch Instruments, Selb, Germany) coupled to a Tensor27 Infrared Spectrometer (Bruker Optics, Ettlingen, Germany) *via* a heated ($T$ = 270 °C) transfer-line. Samples sized 5 mg (*hb*-FR) or 10 mg (epoxy resins, powdered) were heated at a rate of 10 K $min^{-1}$ from 30 to 900 °C under a nitrogen atmosphere *via* gas flow at 30 ml $min^{-1}$. The epoxy resins were powdered using a CryoMill (RETSCH, Germany) under liquid nitrogen.

**Hot-stage-FTIR.** FTIR spectra of the condensed phase during pyrolysis were recorded on a hot-stage FTIR using a Vertex70 FTIR spectrometer (Bruker Optics, Ettlingen, Germany) fitted with an FTIR600 Linkam hot stage cell (Linkam Scientific Instruments Ltd, Chilworth, UK). Powdered samples were pressed into a platelet with potassium bromide as the carrying agent and heated at a rate of 10 K $min^{-1}$ from 30 to 600 °C under a nitrogen purge at 300 ml $min^{-1}$. The scan resolution was 0.4 $cm^{-1}$ and samples were measured between 4000 and 400 $cm^{-1}$.

**LOI.** Limiting oxygen index measurements were performed in accordance with ISO 4589-2. The samples corresponded to type IV of the standard (dimensions: 130 mm × 6.5 mm × 3 mm). All samples were stored at 23 °C and 50% relative humidity for at least 80 hours before measurements.

**UL-94.** Underwriter's Laboratory 94 measurements were performed on samples stored at 23 °C and 50% relative humidity for at least 80 hours in vertical and horizontal orientation according to EN 60695-11-10. The samples were sized 125 mm × 13 mm × 3 mm.

**Cone calorimetry.** All forced-flaming measurements were performed on a cone calorimeter (Fire Testing Technology Ltd, East Grinstead, UK) using a heat flux of 50 kW $m^{-2}$ on samples sized 100 mm × 100 mm × 4 mm, conditioned for at least 48 hours at 23 °C and 50% relative humidity, in accordance with ISO 5660 thus simulating a developing fire.[49] As the standard distance of 25 mm caused the sample residues to touch the heating coil due to intumescence, thus interfering with the measurement results, a distance to the cone heater of 35 mm was chosen.[51] The measurements were conducted in duplicate, and a third measurement was performed if the margin of error was greater than 10%.

**Elemental analysis.** All cone calorimetry residue samples were ground into powder with a mortar and pestle for homogenization purposes and approx. 5 g of material was collected. All elemental analysis measurements were performed by Mikroanalytisches Labor Kolbe (c/o Fraunhofer Institut UMSICHT, Oberhausen, Germany). Phosphorus-contents were determined chromatographically *via* a UV/VIS Specord 90 (Analytik Jena AG, Jena, Germany). For statistical purposes, all measurements were repeated twice.

**SEM.** Scanning electron microscopy measurements were performed on a Zeiss EVO MA10 (Card Zeiss AG, Oberkochen, Germany) using an acceleration voltage of 10 kV. The samples were glued to the sample holder, and then sputtered with gold prior to measurements to avoid charging effects.

**Py-GC-MS.** Pyrolysis gas chromatography/mass spectrometry measurements were conducted using a micro-furnace double-shot pyrolyzer (PY3030iD, Frontier Laboratories, Japan) connected *via* a split/splitless inlet port to a gas chromatograph (7890B, Agilent Technologies, USA) combined with a mass selective detector (5977B, Agilent Technologies, USA). The scan range was 15–550 amu and the EI ionization energy of the MSD was 70 eV. *Via* gravimetric fall into the pyrolysis zone ($T$ = 500 °C), 300 μg samples were pyrolyzed under a helium atmosphere. Using an Ultra Alloy±5 capillary column ($l$ = 30 m, iD = 0.25 mm, film thickness = 0.25 μm), all evolved pyrolysis products were separated under a helium flow of 1 ml $min^{-1}$. The column temperature was held at $T$ = 40 °C for 120 s, then increased at a rate of 10 K $min^{-1}$ to $T$ = 300 °C and held there for 10 min. The GC injector temperature was $T$ = 300 °C and it was operated in a split mode of 1 : 300. Peak assignments were made using the NIST14 MS library as a reference.

**Synthesis of *hb*-polyphosphoramide (1), *hb*-polyphosphorodiamidate (2), *hb*-polyphosphoramidate (3), and *hb*-polyphosphate (4).** **1**, **2**, **3** and **4** were prepared by a radical thiol–ene polyaddition (Scheme 1). For **1**, **2**, and **3**, 234 mmol of the previously synthesized monomer[31] (1 eq.) and 16.7 g of 1,2-ethanedithiol (177 mmol; 0.76 eq.) were dissolved in 240 ml *N*,*N*-dimethylformamide and added to a reactor fitted with a mechanical stirrer under an argon atmosphere. As a radical initiator, 690.5 mg azobisisobutyronitrile (AIBN) (4.1 mmol; 0.02 eq.) was used. For **4**, 80.00 g of **4** (232 mmol; 1 eq.) and 16.57 g of 1,2-ethanedithiol (176 mmol; 0.75 eq.) were dissolved in 240 ml toluene and added to a reactor fitted with a mechanical stirrer under an argon atmosphere. For **2**, **3**, and **4**, 686.5 mg of AIBN (4.18 mmol; 0.02 eq.) was used as a radical initiator, and for **1**, 686.5 mg of AIBN (4.18 mmol; 0.02 eq.) was used. The solution was heated at 100 °C for 24 hours. The crude mixture was then concentrated at reduced pressure. **3** and **4** were precipitated twice into toluene. **1** and **2** were precipitated twice into *n*-hexane. Finally, the polymers were dried at reduced pressure until constant weight (yield **2**, **3**, **4**: 73 g,

76%; yield **1**: 86 g, 89%). The purity and chemical structure were determined by $^{1}$H NMR and $^{31}$P {H} NMR spectroscopy.

### Structure characterization

***hb*-Polyphosphoramide (1).** $^{1}$H NMR (300 MHz, chloroform-*d*): $\delta$ [ppm] = 5.84–5.71 (m); 5.02–4.94 (m); 4.02 (m); 2.70 (s); 2.54 (t); 2.06 (td); 1.69 (m); 1.59 (m); 1.40 (m); 1.39 (m); (Fig. 1a).

$^{31}$P {H} NMR (121 MHz, chloroform-*d*1): $\delta$ [ppm] = −0.66 (s) (Fig. S4†).

***hb*-Polyphosphorodiamidate (2).** $^{1}$H NMR (300 MHz, chloroform-*d*): $\delta$ [ppm] = 5.85–5.72 (m); 5.03–4.93 (m); 3.98 (m); 2.87 (br); 2.70 (s); 2.64 (br); 2.54 (t); 2.06 (td); 1.70–1.36 (m); (Fig. S1†).

$^{31}$P {H} NMR (121 MHz, chloroform-*d*): $\delta$ [ppm] = 9.24 (s) (Fig. S5†).

***hb*-Polyphosphoramidate (3).** $^{1}$H NMR (300 MHz, chloroform-*d*): $\delta$ [ppm] = 5.84–5.71 (m); 5.04–4.93 (m); 3.93 (m); 2.87 (br); 2.70 (s); 2.54 (t); 2.07 (td); 1.64–1.25 (m); (Fig. S2†).

$^{31}$P {H} NMR (121 MHz, chloroform-*d*): $\delta$ [ppm] = 15.49 (s) (Fig. S6†).

***hb*-Polyphosphate (4).** $^{1}$H NMR (300 MHz, chloroform-*d*): $\delta$ [ppm] = 5.85–5.72 (m); 5.03–4.93 (m); 2.88 (br); 2.70 (s); 2.54 (t); 2.07 (td); 1.58–1.24 (m); (Fig. S3†).

$^{31}$P {H} NMR (121 MHz, chloroform-*d*): $\delta$ [ppm] = 17.13 (s) (Fig. S7†).

**Preparation of FR thermosets.** The polymer resin was based on diglycidyl ether of bisphenol A (DGEBA) (Araldite MY740, Bodo Müller Chemie GmbH, Offenbach am Main, Germany) and the amine component 2,2′-dimethyl-4,4′-methylene-bis-(cyclohexylamine) (DMC) (Sigma Aldrich Co. LLC/Merck KgaA, Darmstadt, Germany). The needed ratios of DGEBA and DMC (see Table 2) were calculated using epoxy equivalent weights (ratio 100 : 35), and 10 wt% of the total batch size was replaced with *hb*-FRs or the benchmark FR Bisphenol A bis(diphenyl phosphate) (BDP) (ICL-IP, Tel-Aviv, Israel). All samples needed for measurements were prepared in one batch in the following manner: the respective *hb*-FR was placed in a 1 L polypropylene cup, then DGEBA was added and the chemicals were blended with a wooden spatula until they became homogeneous. DMC was added, and the mixture was thoroughly mixed. Any resulting bubbles were removed *in vacuo*. The compounds were poured into prepared aluminum molds, and then cured in an oven at 90 °C for 30 minutes, at 120 °C for 30 minutes, and at 150 °C for 1 hour. UL-94 and LOI samples were cut into specified dimensions and stored under climate control prior to testing for at least 48 hours according to the respective standards.

Table 2 Composition of FR thermosets

| | Content [g] | | | | |
|---|---|---|---|---|---|
| Material | EP | EP-**1** | EP-**2** | EP-**3** | EP-**4** |
| DGEBA | 222.2 | 200 | 200 | 200 | 200 |
| DMC | 77.8 | 70 | 70 | 70 | 70 |
| 1 | — | 30 | — | — | — |
| 2 | — | — | 30 | — | — |
| 3 | — | — | — | 30 | — |
| 4 | — | — | — | | 30 |

## Conclusions

Phosphorus-containing hyperbranched polymers for use as multifunctional flame-retardant additives for epoxy resins were synthesized *via* $A_2 + B_3$ thiol–ene polymerization. A systematic library of P–O and P–N containing polymers allowed the adjustment of the decomposition mechanism. Results from DSC and TGA experiments showed that $T_g$ and residue yield after pyrolysis increased linearly with the N-content of the *hb*-FRs, and those FRs with a higher N-content were thermally more stable than those with a higher O-content. This was determined to result from a change in the decomposition mechanism which was proposed herein, and that a crucial O : N-ratio determined the pathway. Investigations of flame-retardant epoxy resins provided further evidence of the shift in the chemical decomposition mechanism and ultimately mode of action: all materials exhibited a condensed phase mechanism, as exemplified by the appearance of P-signals in hot stage FTIR measurements, the increase in residue yields in cone calorimeter measurements, and the high amount of the P-content in these residues as determined by elemental analysis. However, *hb*-FRs with a higher O-content exhibited a stronger reduction in the effective heat of combustion, signifying a more pronounced gas phase mechanism. This was supported by CO-yield comparison (see the ESI†) which showed that *hb*-FRs with a higher N-content more strongly affected the combustion efficiency. SEM and residue analysis also illustrated the intumescent characteristic of these FR additives. All *hb*-FRs were compared to the benchmark FR BDP and the results from all measurements demonstrated the ability of these aliphatic FRs to perform at a similar or superior level to an aromatic compound, even at low loadings (P-content in EP < 1%). The *hb*-FRs' ability to mitigate some of the drawbacks of low molecular weight aliphatic FR additives, such as high volatility, low miscibility, poor cohesion in the matrix (leaching or blooming), or strong impact on $T_g$, speaks for their practical use as multifunctional flame retardant additives and showcases the enormous potential hyperbranched polymers can have in developing future materials in the field of flame retardancy.

## Conflicts of interest

There are no conflicts to declare.

## Acknowledgements

The authors thank the Deutsche Forschungsgemeinschaft (DFG) for funding (DFG SCHA 730/15-1; WU 750/8-1).

 

Alexander Battig thanks Patrick Klack for his assistance with the cone calorimeter measurements, Martin Günther, and Michael Morys for their help with SEM images, Dr Katharina Kebelmann for her help with Py-GC-MS measurements, and Letícia V. Lima for her aid in sample preparation and measurements. Jens C. Markwart is the recipient of a fellowship through funding of the Excellence Initiative (DFG/GSC 266) in the context of the graduate school of excellence "MAINZ" (Materials Science in Mainz"). Frederik R. Wurm and Jens C. Markwart thank Prof. Dr Katharina Landfester (MPI-P, Germany). Open Access funding provided by the Max Planck Society.

## Notes and references

1 S. Shaw, *Rev. Environ. Health*, 2010, **25**, 261–306.
2 M. M. Velencoso, A. Battig, J. C. Markwart, B. Schartel and F. R. Wurm, *Angew. Chem., Int. Ed.*, 2018, **57**, 10450–10467.
3 X. Wang, W. Xing, X. Feng, B. Yu, L. Song and Y. Hu, *Polym. Chem.*, 2014, **5**, 1145–1154.
4 S. V. Levchik and E. D. Weil, *J. Fire Sci.*, 2006, **24**, 345–364.
5 B. Perret, B. Schartel, K. Stöß, M. Ciesielski, J. Diederichs, M. Döring, J. Krämer and V. Altstädt, *Eur. Polym. J.*, 2011, **47**, 1081–1089.
6 M. Rakotomalala, S. Wagner and M. Döring, *Materials*, 2010, **3**, 4300–4327.
7 G. Camino, L. Costa and M. P. Luda di Cortemiglia, *Polym. Degrad. Stab.*, 1991, **33**, 131–154.
8 S. K. Brauman, *J. Fire Retard. Chem.*, 1977, **4**, 38–58.
9 B. Perret, K. H. Pawlowski and B. Schartel, *J. Therm. Anal. Calorim.*, 2009, **97**, 949–958.
10 K. H. Pawlowski and B. Schartel, *Polym. Int.*, 2007, **56**, 1404–1414.
11 B. I. Voit and A. Lederer, *Chem. Rev.*, 2009, **109**, 5924–5973.
12 C. J. Hawker, R. Lee and J. M. J. Frechet, *J. Am. Chem. Soc.*, 1991, **113**, 4583–4588.
13 A. Sunder, R. Hanselmann, H. Frey and R. Mülhaupt, *Macromolecules*, 1999, **32**, 4240–4246.
14 C. Chen, G. Liu, X. Liu, S. Pang, C. Zhu, L. Lv and J. Ji, *Polym. Chem.*, 2011, **2**, 1389–1397.
15 R. Hu, J. W. Y. Lam, J. Liu, H. H. Y. Sung, I. D. Williams, Z. Yue, K. S. Wong, M. M. F. Yuen and B. Z. Tang, *Polym. Chem.*, 2012, **3**, 1481–1489.
16 S. E. Stiriba, H. Frey and R. Haag, *Angew. Chem., Int. Ed.*, 2002, **41**, 1329–1334.
17 M. Calderon, M. A. Quadir, S. K. Sharma and R. Haag, *Adv. Mater.*, 2010, **22**, 190–218.
18 K. Y. Pu, K. Li, J. B. Shi and B. Liu, *Chem. Mater.*, 2009, **21**, 3816–3822.
19 P. Y. Wen, X. F. Wang, W. Y. Xing, X. M. Peng, B. Yu, Y. Q. Shi, G. Tang, L. Song, Y. Hu and R. K. K. Yuen, *Ind. Eng. Chem. Res.*, 2013, **52**, 17015–17022.
20 J. Li, C. H. Ke, L. Xu and Y. Z. Wang, *Polym. Degrad. Stab.*, 2012, **97**, 1107–1113.
21 K. C. Cheng, C. C. Wang, J. L. Ruan, C. H. Wu and C. W. Li, *Polym. Adv. Technol.*, 2018, **29**, 2529–2536.
22 L. Zang, S. Wagner, M. Ciesielski, P. Müller and M. Döring, *Polym. Adv. Technol.*, 2011, **22**, 1182–1191.
23 B. Schartel and J. H. Wendorff, *Polym. Eng. Sci.*, 1999, **39**, 128–151.
24 F. Wurm and H. Frey, in *Polymer Science: A Comprehensive Reference*, ed. K. Matyjaszewski and M. Möller, Elsevier, Amsterdam, 2012, ch. 6.05, vol. 6, pp. 177–198.
25 D. H. Zhang, H. Y. Wu, T. C. Li, A. Q. Zhang, Y. L. Peng and F. X. Jing, *Polym. Compos.*, 2011, **32**, 36–43.
26 X. L. Chen, C. M. Jiao, S. X. Li and J. Sun, *J. Polym. Res.*, 2011, **18**, 2229–2237.
27 L. J. Duan, H. Y. Yang, L. Song, Y. B. Hou, W. Wang, Z. Gui and Y. Hu, *Polym. Degrad. Stab.*, 2016, **134**, 179–185.
28 Z. Li, P. Wei, Y. Yang, Y. G. Yan and D. A. Shi, *Polym. Degrad. Stab.*, 2014, **110**, 104–112.
29 S. Gaan, G. Sun, K. Hutches and M. H. Engelhard, *Polym. Degrad. Stab.*, 2008, **93**, 99–108.
30 G. F. Levchik, Y. V. Grigoriev, A. I. Balabanovich, S. V. Levchik and M. Klatt, *Polym. Int.*, 2000, **49**, 1095–1100.
31 J. C. Markwart, A. Battig, L. Zimmermann, M. Wagner, J. Fischer, B. Schartel and F. R. Wurm, *ACS Appl. Polym. Mater.*, 2019, **1**, 1118–1128.
32 H. Chen and J. Kong, *Polym. Chem.*, 2016, **7**, 3643–3663.
33 T. Emrick, H. T. Chang and J. M. J. Frechet, *Macromolecules*, 1999, **32**, 6380–6382.
34 M. Ciesielski, B. Burk, C. Heinzmann and M. Döring, in *Novel Fire Retardant Polymers and Composite Materials*, ed. D.-Y. Wang, Woodhead Publishing, 2017, ch. 2, pp. 3–51, DOI: 10.1016/B978-0-08-100136-3.00002-9.
35 J. Deng and W. F. Shi, *Eur. Polym. J.*, 2004, **40**, 1137–1143.
36 K. Täuber, F. Marsico, F. R. Wurm and B. Schartel, *Polym. Chem.*, 2014, **5**, 7042–7053.
37 F. L. Meng, S. X. Zheng and T. X. Liu, *Polymer*, 2006, **47**, 7590–7600.
38 L.-H. Lee, *J. Polym. Sci., Part A: Gen. Pap.*, 1965, **3**, 859–882.
39 D. P. Bishop and D. A. Smith, *J. Appl. Polym. Sci.*, 1970, **14**, 205–223.
40 B. Schartel, B. Perret, B. Dittrich, M. Ciesielski, J. Krämer, P. Müller, V. Altstädt, L. Zang and M. Döring, *Macromol. Mater. Eng.*, 2016, **301**, 9–35.
41 U. Braun, A. I. Balabanovich, B. Schartel, U. Knoll, J. Artner, M. Ciesielski, M. Döring, R. Perez, J. K. W. Sandler, V. Altstädt, T. Hoffmann and D. Pospiech, *Polymer*, 2006, **47**, 8495–8508.
42 M. Steinmann, M. Wagner and F. R. Wurm, *Chem. - Eur. J.*, 2016, **22**, 17329–17338.
43 J. W. Lyons, *J. Fire Flammability*, 1970, **1**, 302–311.
44 B. Schartel, *Materials*, 2010, **3**, 4710–4745.
45 S. V. Levchik, in *Flame Retardant Polymer Nanocomposites*, ed. A. B. Morgan and C. A. Wilkie, John Wiley & Sons, Inc., 2006, pp. 1–29, DOI: 10.1002/9780470109038.ch1.
46 E. D. Weil, *Fire Retard. Polym. Mater.*, 2000, 115–145.

47 S. V. Levchik, G. F. Levchik, A. I. Balabanovich, E. D. Weil and M. Klatt, *Angew. Makromol. Chem.*, 1999, **264**, 48–55.
48 R. Lyon, in *Handbook of Building Materials for Fire Protection*, ed. C. Harper, McGraw-Hill, New York, New York, 2004, pp. 3.1–3.51.
49 B. Schartel and T. R. Hull, *Fire Mater.*, 2007, **31**, 327–354.
50 R. Petrella, *J. Fire Sci.*, 1994, **12**, 14–43.
51 B. Schartel, M. Bartholmai and U. Knoll, *Polym. Degrad. Stab.*, 2005, **88**, 540–547.